Exceptional Hardness and Thermal Properties of SiC/(Hf,Ta)C(N)/(B)C Ceramic Composites Derived from Single-Source Precursor

Jan Bernauer,* Nils-Christian Petry, Nathalie Thor, Samuel Aeneas Kredel, Dharma Teja Teppala, Mathias Galetz, Maren Lepple, Astrid Pundt, Emanuel Ionescu, and Ralf Riedel

In the present work, monolithic SiC/(Hf$_{0.75}$Ta$_{0.25}$)C(N)/(B)C ceramic composites are prepared via spark plasma sintering of amorphous SiHfTa(B)CN-based powders synthesized from single-source precursors. The as-sintered ceramic nanocomposites are investigated by X-ray diffraction, Raman, scanning electron microscopy, and transmission electron microscopy in order to study their microstructure and chemical composition. Furthermore, the thermal conductivity, the thermal expansion, as well as the hardness and Young's moduli of the prepared monolithic samples are determined. The incorporation of boron in the system results in enhanced densification due to decreased porosity and improved distribution of the individual phases in the composite after sintering. These favorable effects also positively influence the thermomechanical properties of the composite. The boron-modified sample displays a decreased thermal diffusivity and conductivity compared with the boron-free sample. Additionally, a macrohardness obtained by Vickers indentation of 31 GPa is achieved for loads up to 196 N, surpassing the hardness of ultrahard materials like silicon carbide, hafnium carbide, and tantalum carbide as well as their solid solutions. Young's moduli of the composites were analyzed to 405 ± 10 and 277.5 ± 41 GPa for the boron-containing and boron-free samples, respectively.

1. Introduction

Hafnium carbide (HfC) and tantalum carbide (TaC) display melting points of more than 3800 °C, whereby the solid solution with the composition of Hf$_{0.2}$Ta$_{0.8}$C is considered the compound with the highest known melting point of ≈3990 °C.[1,2] Together with selected borides, carbides, and nitrides of group IV and V transition metals, they form the family of ultrahigh temperature ceramics (UHTCs).[3–5] Their excellent thermal stability enables them to operate at temperatures beyond the capabilities of traditional materials, making them promising candidates for high-temperature thermal protection systems or functional components for hypersonic flight vehicles.[6,7] Furthermore, they are classified by their high hardness, chemical inertness, and good resistance to thermal shock.[8,9] However, densification of UHTC materials typically requires temperatures above 50% of their melting point.[10,11] Moreover, UHTCs exhibit rather high oxidation kinetics at moderate temperatures. For instance, hafnium carbide starts to oxidize at a temperature of 550 °C, forming a porous hafnium oxide scale, which fails as a protective scale

J. Bernauer, S. A. Kredel, D. T. Teppala, E. Ionescu, R. Riedel
TU Darmstadt
Institut für Materialwissenschaften
Otto-Berndt-Str. 3, Darmstadt 64287, Germany
E-mail: jan.bernauer@tu-darmstadt.de

N.-C. Petry, M. Galetz, M. Lepple
DECHEMA-Forschungsinstitut
High Temperature Materials
Theodor-Heuss-Allee 25, Frankfurt am Main 60486, Germany

N. Thor
Technische Universität Darmstadt
Institut für Angewandte Geowissenschaften
Schnittspahnstraße 9, Darmstadt 64287, Germany

M. Lepple
Justus Liebig Universität Gießen
Institut für Anorganische und Analytische Chemie
Heinrich-Buff-Ring 17, Gießen 35392, Germany

A. Pundt
Karlsruhe Institut für Technologie
Institut für Angewandte Materialien – Werkstoffkunde
Engelbert-Arnold Straße 4, Karlsruhe 76131, Germany

E. Ionescu
Fraunhofer-Einrichtung für Werkstoffkreisläufe und Ressourcenstrategie IWKS
Brentanostraße 2a, Alzenau 63755, Germany

and can potentially lead to the destruction of extensive components.[12–14] Tantalum carbide forms Ta_2O_5, melting at a temperature of 1872 °C.[2] The classical approach to improve the oxidation resistance of UHTC materials is the addition of a supportive silica former, as done in HfB_2/SiC and ZrB_2/SiC composites with 20 vol% SiC.[12,15] The presence of a silica-forming phase improves the oxidation resistance of UHTCs by forming a protective scale expected to protect the UHTC up to 1600 °C.[15,16] A sophisticated method to synthesize silica-forming composites is the polymer-derived ceramic (PDC) route.[17,18] The method allows chemically modifying silicon-containing polymers with organometallic compounds to form, after a thermal treatment, UHTC composites. In previous studies, monolithic UHTC (nano)composites were synthesized from amorphous SiHfTaC(N) powders by spark plasma sintering (SPS), leading to multiphase composites with the composition of SiC/(Hf,Ta)C(N)/C.[19,20] Due to the cubic rocksalt-type structure (NaCl type) of both carbides and nitrides of hafnium and tantalum and their almost complete miscibility at high temperatures (2000 °C), a solid solution of HfC(N) and TaC(N) was formed.[21,22] The ceramic composites, especially the composition with the adjusted Hf:Ta ratio of 7:3, showed an enhanced high-temperature oxidation resistance by forming a continuous oxidation scale consisting not only of silica but also of $Hf_6Ta_2O_{17}$.[23,24] The binary oxide exhibits no phase transformations up to 2500 °C, making it an ideal material for high-temperature applications.[23–25] In addition to the parameters mentioned earlier, i.e., melting point and oxidation resistance, additional critical parameters have to be considered and rationalized when materials are anticipated to operate at high and ultrahigh temperatures. For example, the thermal expansion, appropriate thermal conductivity, resistance to localized plastic deformation, or modulus of elasticity as UHTC composites can suffer from thermal stresses induced by different thermal expansion coefficients of their specific phases.[26,27] The morphology and distribution of the individual phases, which strongly depend on the processing, can further impair the mechanical performance.[28–30]

In the present work, mechanical and thermal data for monolithic samples derived from polymers were acquired. Therefore, the synthesis of multiphase composites with the composition of SiC/$(Hf_{0.75}Ta_{0.25})$C(N)/(B)C was conducted. Initially, the impact of chemical composition on the microstructure of the sintered samples was investigated. Subsequently, the thermal properties, encompassing thermal expansion, thermal diffusivity, and thermal conductivity, as well as hardness and Young's moduli, were assessed. The observed differences in these properties were elucidated by their correlations with the microstructure.

2. Results and Discussion

2.1. Composition and Microstructure

XRD analysis was conducted on both the powders synthesized at 1000 °C and the monolithic samples prepared via SPS. The corresponding diffractograms are shown in **Figure 1**. The XRD analysis of the powders reveals a predominantly amorphous nature. However, faint reflections are detected, signifying the presence of small quantities of hafnium oxide and silica. The observations
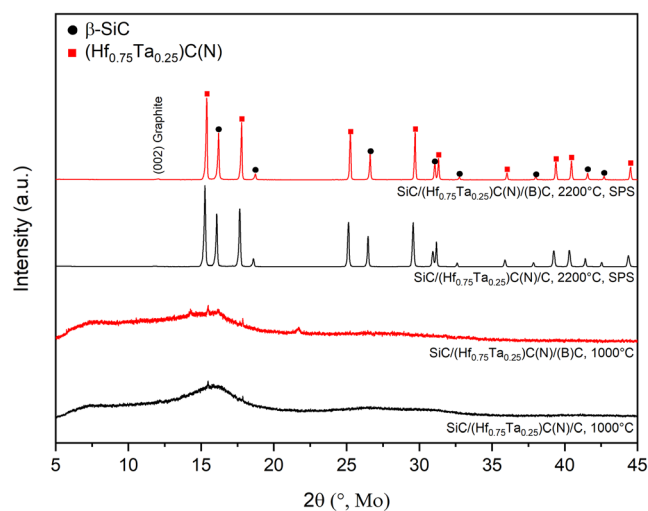

Figure 1. XRD patterns of SiC/$(Hf_{0.75}Ta_{0.25})$C(N)/(B)C and SiC/$(Hf_{0.75}Ta_{0.25})$C(N)/C powders synthesized at 1000 °C and of the corresponding monolithic samples sintered at 2200 °C under SPS conditions.

suggest the occurrence of minor oxygen contamination during the precursor synthesis and/or pyrolysis processes. In contrast, the monolithic samples consolidated using SPS exhibited a high degree of crystallinity. The XRD patterns confirmed the presence of β-SiC, the solid solution $(Hf_{0.75}Ta_{0.25})$C(N), and graphite within the samples. The graphite phase displays a weakly visible reflection of the (002) plane. The phase separation of the spark plasma sintered Si(Hf,Ta)C(N) samples into β-SiC, (Hf,Ta)C(N), and segregated carbon phase has been thoroughly discussed in the literature.[19,31] Notably, no boron-containing crystalline phases are detected. This can be attributed to the possibility that boron has dissolved in the carbon phase instead of forming compounds with hafnium or tantalum. This behavior has been previously reported in the literature.[32]

Raman spectroscopy was performed on bulk samples with and without boron after SPS densification, allowing the analysis of carbon allotropes formed, as well as the crystallinity and distortions of the carbon lattice.[33,34] The spectra are presented in **Figure 2**. The first-order Raman spectra exhibit the T_O band of β-SiC between 790 and 800 cm^{-1} in both samples. This band corresponds to the transverse optical phonon mode of β-SiC. The boron-containing sample displays a more pronounced band, indicating enhanced crystallization of the SiC phase and a larger grain size. This behavior has been previously observed in similar compositions containing only hafnium as a transition metal.[31] Other bands are attributed to the segregated carbon phase present in both monolithic samples. To characterize the nature, hybridization, crystallinity, and ordering of the carbon phase, various Raman bands such as D, G, D′, 2D, D + G, and 2D′ were examined. The most prominent band in all spectra is the E_{2g} symmetric bond stretching band of sp^2-hybridized carbon atoms, labeled as G ($\approx$1585 cm^{-1}). Bands D ($\approx$1356 cm^{-1}) and D′ ($\approx$1630 cm^{-1}) are caused by sp^3 carbon vibrations related to disordered or nanostructured carbon. Bands D + D″ ($\approx$2449 cm^{-1}), 2D ($\approx$2709 cm^{-1}), and 2D′ ($\approx$3250 cm^{-1}), as well as D + D′ ($\approx$2938 cm^{-1}), correspond to the two-phonon modes of the

**ADVANCED
SCIENCE NEWS**

www.advancedsciencenews.com

**ADVANCED
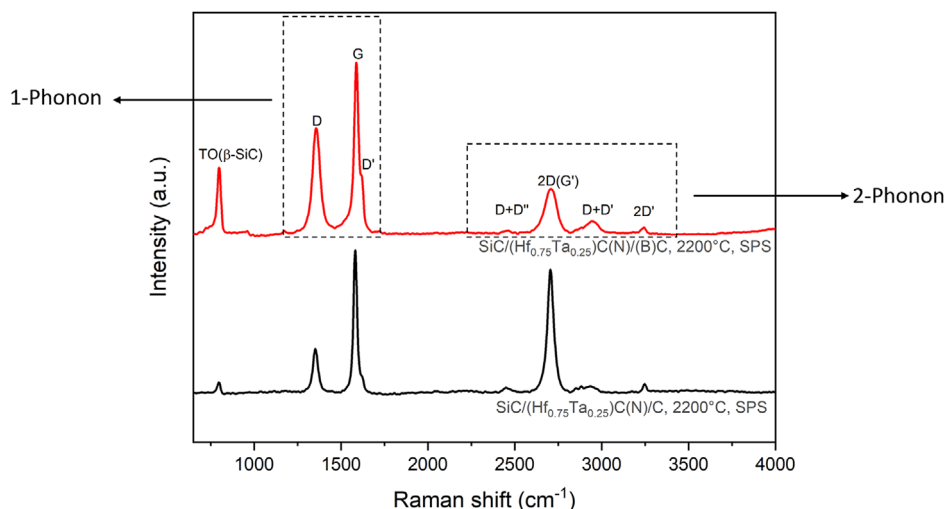ENGINEERING
MATERIALS**

www.aem-journal.com

Figure 2. Raman spectra of SiC/(Hf$_{0.75}$Ta$_{0.25}$)C(N)/(B)C (red) and SiC/(Hf$_{0.75}$Ta$_{0.25}$)C(N)/C (black) sintered at 2200 °C under SPS conditions.

first-order bands. Compared to the boron-free sample, the boron-containing composite displays an enhanced D and D′ band, indicating the incorporation of boron into the graphitic lattice.[35] In the second-order modes, the 2D and G′ overlap is broadened for the boron-containing sample, indicating a disordering of the segregated carbon phase. In contrast, the boron-free material exhibits a less pronounced D and D′ band, indicating a higher degree of graphitization. Furthermore, the merging of the D′ band with the G band is a typical feature of small grains.

In addition to XRD and Raman spectroscopy, elemental analysis was performed on the SiC/(Hf$_{0.75}$Ta$_{0.25}$)C(N)/(B)C powder and bulk sample. **Table 1** displays the chemical composition and empirical formula of the ceramics that were obtained at 1000 °C and sintered at 2200 °C. After sintering, the elemental analysis determined that the Hf:Ta ratio remained constant at 75:25 in both the pyrolyzed powder and the bulk material. The boron concentration does not correspond to the amount set in the single-source precursor. Only approximately 32% of the boron incorporated within the single-source precursor appeared in the pyrolyzed powder. This finding is attributed to steric hindrance and the limited reactivity of the preceramic polymer. Similar behavior has been found in the reaction of vinyl-containing polysilazanes or carbosilanes with the borane dimethylsulfide complex.[31]

Upon sintering, carbon and nitrogen contents decreased, while the oxygen content remained relatively stable. As no oxygen-containing phases, such as silicon oxide or transition metal oxide, were observed in the XRD patterns, it is assumed that the oxygen is present as amorphous silicon oxide. The silicon oxide can either derive from the precursor material even if the plasma sintering was conducted under a reductive atmosphere or

was introduced during the grinding of the bulk samples for elemental analysis. Therefore, the presence of oxygen is neglected in further discussions regarding the mechanical and thermal properties. The empirical formula of SiC/(Hf$_{0.75}$Ta$_{0.25}$)C(N)/C is expected to be similar to that of SiC/(Hf$_{0.75}$Ta$_{0.25}$)C(N)/(B)C, as the only difference is the addition of boron.

The microstructure of the prepared monolithic samples was investigated using high-resolution scanning electron microscopy (HR-SEM). **Figure 3** displays SEM-backscattered electron (SEM-BSE) images of SiC/(Hf$_{0.75}$Ta$_{0.25}$)C(N)/C (left) and SiC/(Hf$_{0.75}$Ta$_{0.25}$)C(N)/(B)C (right). The SEM image of the boron-free sample indicates a relatively high density with visible pores at higher resolutions. The microstructure of the SiC/(Hf,Ta)C(N)/C monolithic bulk ceramic is divided into two microstructural regions. The first region consists of fragments of former powder particles, which contain finely distributed (Hf,Ta)C(N) precipitates and SiC. The (Hf,Ta)C(N) precipitates were formed in situ during sintering within the SiC matrix and have an average grain size of approximately 100 nm, estimated by SEM. The second region is located between these former powder particles, appearing darker in the SEM-BSE images and mainly consisting of SiC. These areas are referred as sinter necks and connect the precipitation-rich particles and originate from the particle surfaces. The addition of boron led to the development of a more refined microstructure characterized by a near absence of discernible pores. The (Hf,Ta)C(N) distribution exhibits a heightened level of uniformity, as exemplified by the SEM analysis presented in the top right SEM image. The analysis through SEM yields an estimated average grain size of 170 nm for the (Hf,Ta)C(N) particles.

Table 1. Chemical composition by mass and empirical formula of the SiB(Hf,Ta)C(N,O) ceramics pyrolyzed at 1000 °C and sintered at 2200 °C.

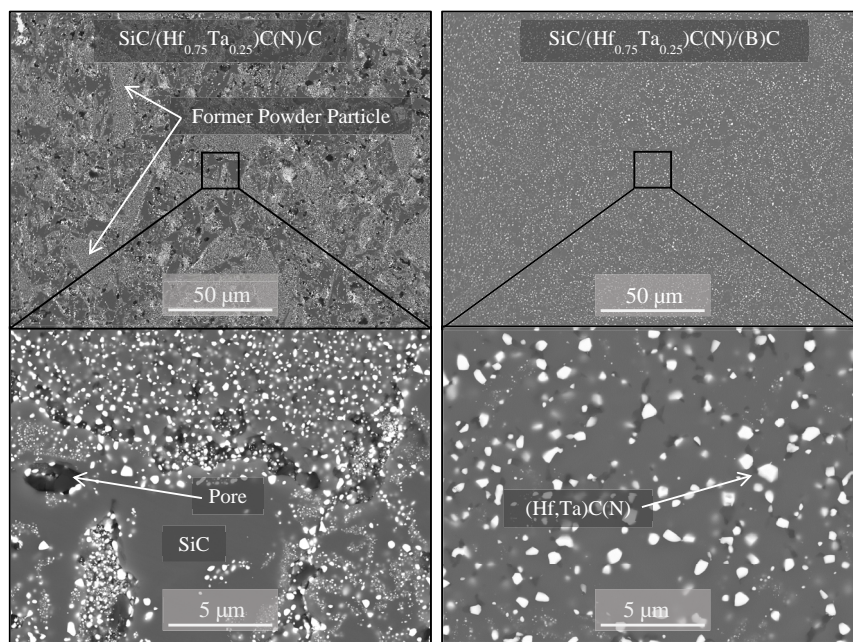| Sample	Elemental Content [wt%]							Empirical Formula
	Si	Hf	Ta	B	C	N	O	
SiC/(Hf$_{0.75}$Ta$_{0.25}$)C(N)/(B)C-1000 °C	45.8	12.4	4.25	0.16	28.00	3.85	4.67	Si(Hf$_{0.043}$Ta$_{0.014}$)B$_{0.01}$C$_{1.43}$N$_{0.17}$O$_{0.18}$
SiC/(Hf$_{0.75}$Ta$_{0.25}$)C(N)/(B)C-2200 °C	49.5	12.8	4.38	0.2	24.52	0.572	4.25	Si(Hf$_{0.041}$Ta$_{0.014}$)B$_{0.01}$C$_{1.16}$N$_{0.02}$O$_{0.15}$

**ADVANCED
SCIENCE NEWS**

www.advancedsciencenews.com

**ADVANCED
ENGINEERING
MATERIALS**

www.aem-journal.com

Figure 3. SEM-BSE images of sintered SiC/(Hf$_{0.75}$Ta$_{0.25}$)C(N)/C and SiC/(Hf$_{0.75}$Ta$_{0.25}$)C(N)/(B)C bulk ceramics showing a difference in the overall microstructure, when comparing both ceramics. The microstructure of the SiC/(Hf$_{0.75}$Ta$_{0.25}$)C(N)/C shows different microstructural regions with former powder particles, sinter necks, and porosity, whereas the microstructure of the SiC/(Hf$_{0.75}$Ta$_{0.25}$)C(N)/(B)C bulk ceramic is homogeneous.

The SEM results are further corroborated by TEM studies, specifically brightfield (TEM-BF) imaging, as illustrated in **Figures 4**a,b. The TEM-BF images in Figure 4a, comprising a composite of 62 individual images, allowed for a more extensive field of view, in contrast to the single TEM-BF image featured in Figure 4b. This compilation of images vividly illustrates the pronounced homogeneity of the microstructure, as expounded in the SEM-BSE image in Figure 3.

Furthermore, Figure 4c shows the respective HR-TEM images and corresponding SAED patterns in addition to the EDS spectra of the two constituting phases: SiC and (Hf,Ta)C(N). In addition, an amorphous carbon shell on top of the hafnium tantalum carbonitride particle is depicted in Figure 4d. SiC occurs in its cubic polymorph 3C-SiC, confirming the findings of the XRD analysis. TEM imaging reveals stacking faults (SFs) in SiC, marked by the bright/dark contrasts in the HR-TEM image and supported by the smearing within the diffraction points in the SAED pattern.

The density and open porosity of the monolithic samples were assessed using the Archimedes method. The results are listed in **Table 2**. Additionally, point counting was used to estimate the total porosity based on SEM image data.[36] As anticipated from SEM imaging (refer to Figure 3), the boron-modified sample generally exhibits enhanced density and reduced levels of open and total porosity compared to that of the boron-free sample. This finding again highlights boron's advantageous impact on the microstructure evolution during SPS.

2.2. Thermal Properties

The thermal conductivity of composite materials is influenced by various factors such as the volume fractions of the phases, grain size, grain distribution, or dispersity and porosity.[37] To describe the temperature-dependent thermal conductivity, Equation (1) is used:

$$\lambda(T) = \alpha(T) \cdot C_{\mathrm{p}}(T) \cdot \rho(T) \tag{1}$$

In Equation (1), $\lambda(T)$ represents the thermal conductivity, $\alpha(T)$ denotes the thermal diffusivity, $C_{\mathrm{p}}(T)$ signifies the heat capacity, and $\rho(T)$ corresponds to the density. The temperature-dependent heat capacity and thermal diffusivity are determined by differential scanning calorimetry and laser flash measurements, respectively. However, estimating the temperature-dependent density requires an alternative approach, which can be achieved using Equation (2):

$$\rho(T) = \rho_0(1 - \beta(T - T_0)) \tag{2}$$

In Equation (2), ρ_0 represents the density at room temperature (RT), T_0 denotes the temperature at RT, and β represents the coefficient of volumetric expansion. Here, a linear behavior of density is assumed. Furthermore, assuming an isotropic behavior of the materials, β can be calculated from the linear thermal expansion coefficient β_{L} ($3\beta = \beta_{\mathrm{L}}$). The thermal expansion coefficient (CTE) of a composite is the combination of the matrix's CTE, which is modified by the influence of the dispersed phase on the expansion of the matrix and vice versa. The thermal expansion coefficient is derived from dilatometry in the temperature range of 100–1500 °C as shown in **Figure 5**.

The average thermal expansion coefficient within the ranges of 100–1000 and 1000–1500 °C, together with the thermal conductivity, diffusivity, and heat capacity, is provided in **Table 3**. In the measured temperature range, the expansion
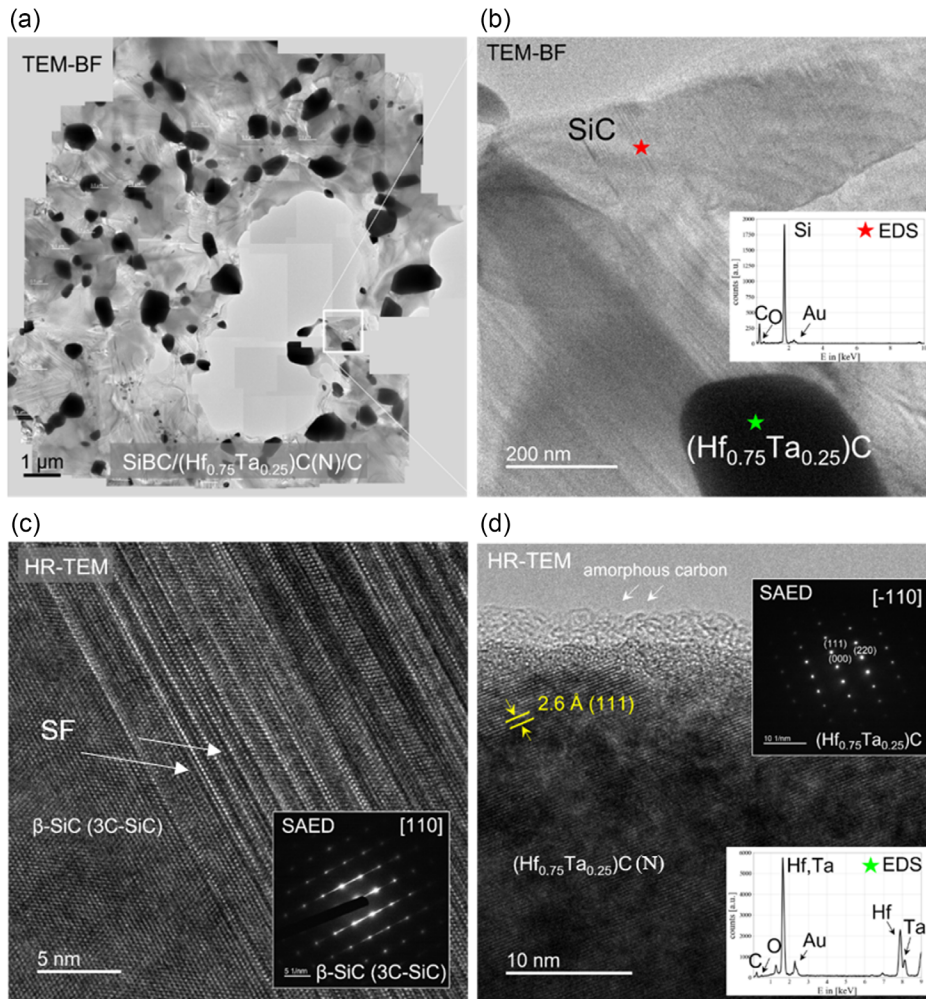
Figure 4. TEM images of sintered SiC/(Hf$_{0.75}$Ta$_{0.25}$)(N)C/(B)C. a,b) Bright-field images. (a) A composite of 62 images to provide an extensive field view. c) HRTEM and the constituting SiC phase and the correlated SEAD pattern, while in d), the amorphous carbon shell on the transition metal carbonitrides is depicted.

Table 2. Density, open porosity, and total porosity of the bulk samples SiC/(Hf$_{0.75}$Ta$_{0.25}$)C(N)/C and SiC/(Hf$_{0.75}$Ta$_{0.25}$)C(N)/(B)C.

Sample	Density [g cm^{-3}][a]	Open porosity [%][a]	Porosity [%][b]
SiC/(Hf$_{0.75}$Ta$_{0.25}$)C(N)/(B)C/C	3.669	0.61	1.85 ± 0.32
SiC/(Hf$_{0.75}$Ta$_{0.25}$)C(N)/C	3.332	1.62	6.83 ± 0.98

[a]Measured by Archimedes method, [b]Determined by assessing ten SEM-BSE images using the thresholding tool within the software ImageJ.

characteristics of the specimens remain uniform and display negligible deviation in their quasi-linear expansion. This minimal deviation can be ascribed not only to the limited compositional variation but also, more significantly, to the microstructural disparities among the samples.

The coefficients of thermal expansion are close to those reported for the most pronounced phases (3C) β-SiC and a solid solution of HfC-TaC.[38,39] For β-SiC values in between 4.3 and
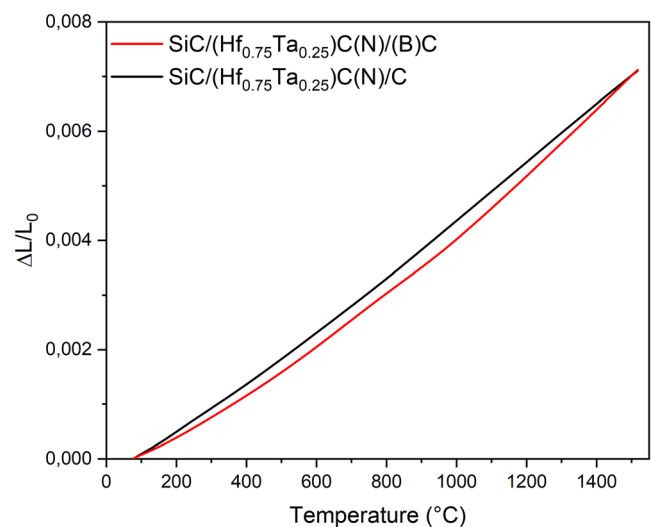

Figure 5. Thermal expansion of the materials were determined by dilatometry in the temperature range of 100–1500 °C.

Table 3. Average thermal conductivity, diffusivity, heat capacity, and thermal expansion coefficient of SiC/(Hf0.75Ta0.25)C(N)/(B)C and SiC/(Hf0.75Ta0.25)C(N)/C.

Sample	Average				
	Thermal conductivity [W m^{-1} K^{-1}] (850 °C)	Thermal diffusivity [mm^2 s^{-1}] (850 °C)	Heat capacity [J g^{-1} K^{-1}] (850 °C)	CTE (10^{-6} K^{-1}) (100–1000 °C)	CTE (10^{-6} K^{-1}) (1000–1500 °C)
SiC/(Hf$_{0.75}$Ta$_{0.25}$)C(N)/(B)C	31.14	8.67	0.97	4.44 ± 0.02	5.98 ± 0.20
SiC/(Hf$_{0.75}$Ta$_{0.25}$)C(N)/C	36.27	11.16	0.99	4.74 ± 0.02	5.32 ± 0.08

6.2×10^{-6} K^{-1} from room temperature to 1400 °C can be found in the literature.[40–42] Li and Brat described the behavior with a second-order polynomial describing the continuous increase from 3.2×10^{-6} K^{-1} at RT to 5.1×10^{-6} K^{-1} at 1000 °C, averaging a value of 4.45 in between this temperature range.[38] The coefficient of thermal expansion of hot-pressed HfC$_{0.96}$ and TaC$_{0.99}$ was measured by Jun and Shaffer[43] from room temperature to 2600 °C in argon. HfC$_{0.96}$ displayed a CTE of 6.19×10^{-6} K^{-1} from RT-1000 and 6.59 up to 1500 °C and TaC$_{0.99}$, respectively, a CTE of 6.61×10^{-6} K^{-1} from RT-1000 and 6.67 up to 1500 °C. For the solid solution of HfC-TaC, a decrease in the coefficient of thermal expansion compared to single carbides was reported by Barantseva and Paderno.[39] The boron-free monolithic sample exhibits a slightly higher CTE value than the boron-modified sample between 100 and 1000 °C. Above this range, the values converge, and the boron-rich sample shows a higher CTE between 1000 and 1500 °C. The slight divergence can be drawn back to the residual porosity, the microstructure, and the different degrees of graphitization of the segregated carbon phase. Pyrolytic carbon displays a CTE between 4 and 6×10^{-6} K^{-1} and depends strongly on the carbon type (especially if disordered by boron).[44]

For thermal conductivity calculations, the temperature dependence of the density given by Equation (2) was neglected for the investigated materials as the volumetric expansion is below 1%. The evolution of the specific heat capacity with the temperature is shown in **Figure 6**. The values are in the expected range and follow the trend of β-SiC.[45] The influence of the other phases is relatively small. At high temperatures, the capacity becomes constant and levels around 1 J g^{-1} K^{-1}, clearly higher than the reported range of 0.2–0.3 J g^{-1} K^{-1} for HfC, TaC, and their solid solutions.[10]

The temperature-dependent thermal diffusivity was measured by laser-flash analysis, and the respective graph is depicted in **Figure 7**. Both samples display a similar trend in the temperature dependence of the thermal diffusivity. At 50 °C, the difference between the samples is high as the boron-containing sample shows a diffusivity of ≈20 mm^2 s^{-1}, while the boron-free sample doubles the diffusivity with ≈40 mm^2 s^{-1}. Both samples show a decrease in the diffusivity with temperature and converge for high temperatures.

From the previous results on the higher open porosity and the (Hf,Ta)C(N) grain size, a lower diffusivity for SiC/(Hf$_{0.75}$Ta$_{0.25}$)C(N)/C would be expected as both factors decrease the diffusivity and the resulting thermal conductivity.[46,47] However, in a multicomponent system, the conductivity first depends on the conductivity of each phase and their distribution. If the highly conductive phase is continuous in the system, the resulting
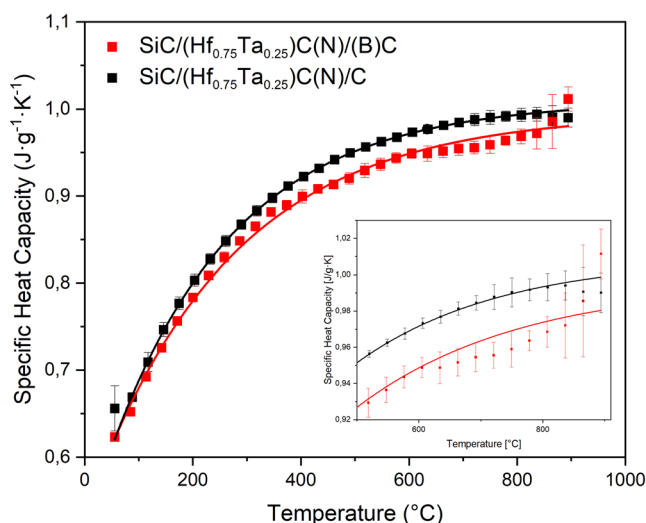

Figure 6. Evolution of the specific heat capacity in the range of RT—900 °C. The magnification shows the constant range at the maximum measured temperature.
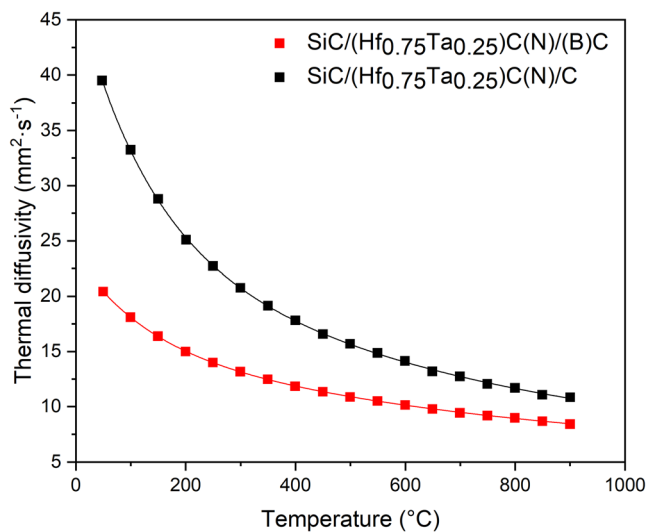

Figure 7. Thermal diffusivity in the range of RT—900 °C.

conductivity is high and vice versa.[37] The main phase β-SiC of the system investigated has a high thermal conductivity depending on the fabrication.[29,46] Nanosized SPS-sintered β-SiC, on the other hand, can show a relatively low thermal
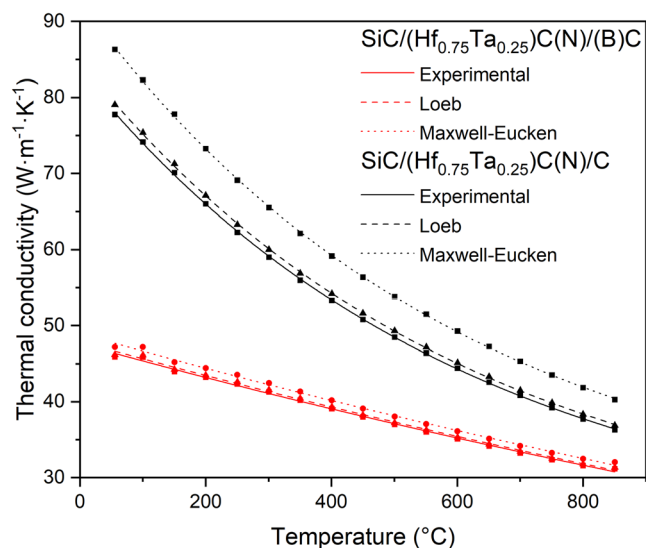
Figure 8. Thermal conductivity from RT—850 °C and the corrected conductivities by Loeb and Maxwell–Eucken.

conductivity for SiC of around 80–100 $W\ m^{-1}\ K^{-1}$, which can be compared well with the results displayed in **Figure 8**.[28,29] The added phases, in this case the (Hf,Ta)C(N) phase, act as scattering points for phonons, decreasing the thermal conductivity in the system.[37] For SiC/(Hf$_{0.75}$Ta$_{0.25}$)C(N)/C, continuous areas with a discrete phase without any dispersed phase (refer to Figure 3) were found, leading to an increased conductivity at low temperatures.

In contrast, SiC/(Hf$_{0.75}$Ta$_{0.25}$)C(N)/(B)C shows well-distributed (Hf,Ta)C(N) precipitations and no discrete SiC phase, resulting in a hindered phonon propagation. Therefore, the lower diffusivity and conductivity as compared to the boron-free sample result from the different microstructures related scattering effect, predominant especially in the low-temperature range. At high temperatures, both the diffusivity and conductivity values approach each other, and the conductivity difference is only about 6 $W\ m^{-1}\ K^{-1}$.

In order to counteract the effect of open and closed porosity and thereby make the results more comparable, two corrections were applied. First, the impact of the open porosity was calculated by the approach that solid and pore phases act as thermal resistors in parallel. Equation (3), which is also known as the rule of the mixture, is valid under the assumption that the phases do not interact with each other, which allows us to calculate the effective thermal conductivity λ_s of the solid.[47]

$$\lambda = \lambda_s(1 - \nu_p) + \nu_p \lambda_p \tag{3}$$

where λ is the experimental thermal conductivity, λ_p is the pore thermal conductivity, and ν_p is the pore volume fraction. If $\lambda_p \ll \lambda_s$, we can assume $\lambda_p = 0$, which leads to Loeb's relation, Equation (4).[48]

$$\lambda^* = \lambda_s(1 - \nu_p) \tag{4}$$

For the calculation, the open porosity values obtained by the Archimedes principle and the effective thermal conductivity λ

obtained by the measurement were used. The second correction in which the closed porosity is considered can be carried out with the Maxwell–Eucken equation. Equation (5) describes the thermal conductivity when the closed porosity is below a limit of 15%.[47]

$$\lambda = \lambda_s \frac{\lambda_p + 2\lambda_s + 2\nu_p(\lambda_p - \lambda_s)}{\lambda_p + 2\lambda_s - \nu_p(\lambda_p - \lambda_s)} \tag{5}$$

The closed porosity values obtained by several SEM measurements were used for the calculation (refer to chapter 3.1). The corrections made by the Maxwell–Eucken equation for the closed porosity significantly influence the solid's thermal conductivity for the boron-free samples displayed in Figure 8. The correction on the boron-modified sample is relatively small caused by the low porosity. After the two corrections, the deviation of the two samples is now 8 $W\ m^{-1}\ K^{-1}$ at the highest measured temperature (850 °C) and slightly greater at low temperatures. In general, one can conclude that the difference in composition and microstructure of the two samples strongly influence the thermal conductivity at low temperatures, while at high temperatures, the influence is less pronounced. This finding is discussed in terms of the predominant electronic contribution of the thermal conductivity at high temperatures, while at low temperatures, the phononic part of the thermal conductivity is pronounced, especially in the SiC phase, due to its strong and rigid atomic structure.[10]

2.3. Mechanical Properties

The synthesized composite materials studied in the present work consist of individual phases denoted already as carbide-based ultra-hard materials.[8] Various values for the different carbides depending on the type of hardness measurement (nano, micro, or macro indentation) and microstructure (grain size and porosity) obtained by different sintering processes can be found in the literature.[49,50] Dense, SPS sintered silicon carbide (β-SiC) displays an exceptionally high micro-hardness of up to 32 GPa,[50] while liquid phase sintered SiC shows a micro-hardness of 20–28 GPa.[51] The monocarbides of HfC and TaC display a lower micro-hardness of 18.5[22] and 12–19 GPa,[22,52] respectively. For the solid solutions of (Hf$_{0.75}$Ta$_{0.25}$)C, higher values of 19–29 GPa have been reported.[22,53] The Hf/Ta substitution in the metallic sublattice introduces some degree of distortion and creates analogous to solid solution strengthening in alloys' local stress fields, increasing the hardness. Furthermore, the addition of Ta in HfC promotes a change in the shift in the slip plains, further causing a higher hardness.[53] The solid solution further shows excellent flexural strength at elevated temperatures, displayed for the composition of Hf$_{0.2}$Ta$_{0.8}$.[54] Young's moduli of SiC are in the range of 400–450 GPa[50,55] and those of the transition metal carbides range between 300 and 600 GPa.[8,22]

For the examined composites, hardness and Young's moduli akin to, or possibly exceeding, those of the monolithic carbides were anticipated.[56,57] In the Vickers and nanoindentation experiments, substantial loads were employed to capture a comprehensive depiction of the entire microstructure rather than isolated phases. Furthermore, by varying the applied load, we
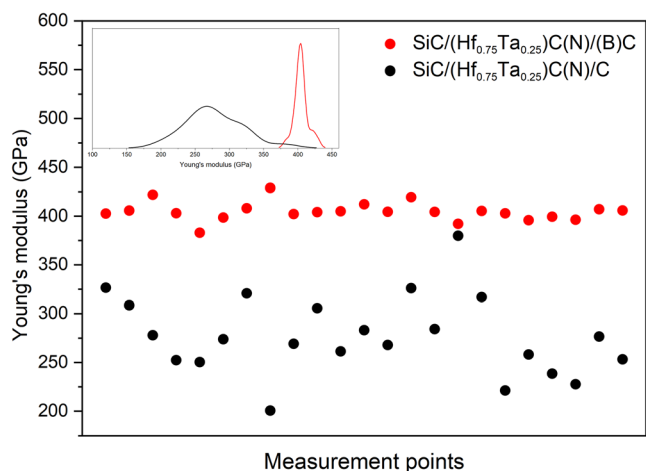
Figure 9. Young's moduli obtained by a test grid of 5 × 5 measurements and the resulting distribution of moduli.

sought to mitigate any potential indentation size effects. The Young's moduli were determined by nanoindentation experiments using the technique developed by Oliver and Pharr.[58] The determined Young's moduli are displayed in **Figure 9**, where the microstructural influence is once more clearly visible. The obtained values for the boron-modified specimen are narrowly distributed with a mean modulus of 405 ± 11 GPa with a low variance displayed in the coefficient of variation of 2.5%. The boron-free sample, on the other hand, shows a lower modulus of 278 ± 41 GPa with a considerable variation in the results (coefficient of variation of 14.6%). It should be considered that the relatively high loads used for the experiments may indeed lead to fracture development in the boron-free sample, highlighting the impact of the porosity and inhomogeneity in the microstructure and on the material's performance.

The variation can be further analyzed by investigating the load–displacement curves (L-D curves) of the indentation experiments. **Figure 10** displays the load displacement curves

of SiC/(Hf$_{0.75}$Ta$_{0.25}$)C(N)/C (**left**) and SiC/(Hf$_{0.75}$Ta$_{0.25}$)C(N)/(B)C (**right**). Three exemplary curves have been depicted in order to keep the presentation clear.

The load–displacement (L-D) curves for the boron-modified sample exhibit a consistently smooth nature, with overlapping curves implying a consistent response across the entire bulk sample. Occasionally, small pop-in or pop-out events were observed, characterized by an abrupt increase in displacement during constant load. These events are often attributed to the transition from elastic deformation to elastic-plastic deformation resulting from phase transformations induced by contact stresses, as observed in silicon.[59–61] In porous materials, these events can not only be ascribed to phase transformations but, more commonly, to cracking.[61] A schematic representation of the indentation experiment, illustrating pore cracking and larger deformations, is depicted in **Figure 11** (left), alongside a depiction of the behavior of the boron-modified sample (right). In the boron-containing sample, the observation of only minor events can be attributed to slight disruptions on the surface. Conversely, the L-D curve of the SiC specimen displays significant variance in the loading and unloading curves, with numerous marked pop-in and pop-out events denoted by black arrows (major pop-ins) and green arrows (minor pop-ins). Minor pop-in events exhibit rapid increases in displacement followed by a more gradual ascent, while major pop-in events are discernible due to their prolonged displacement increments. Both types of events occur recurrently and are attributed to the heterogeneous nature of the sample, leading to fracture development during loading.

Vickers hardness measurements were conducted over a load range spanning from 196.13 to 19.61 N, encompassing macrohardness values. The results of these measurements and a post-indentation image at 196.13 N are illustrated in **Figure 12**. Notably, the SiC/(Hf$_{0.75}$Ta$_{0.25}$)C(N)/C ceramics exhibit an asymptotic load-dependent behavior, with the highest recorded hardness value of 22.4 ± 3.6 GPa achieved at the lowest load. With increasing load, the hardness gradually decreases to 14.4 ± 0.9 GPa at 196.13 N, revealing an overall indentation size
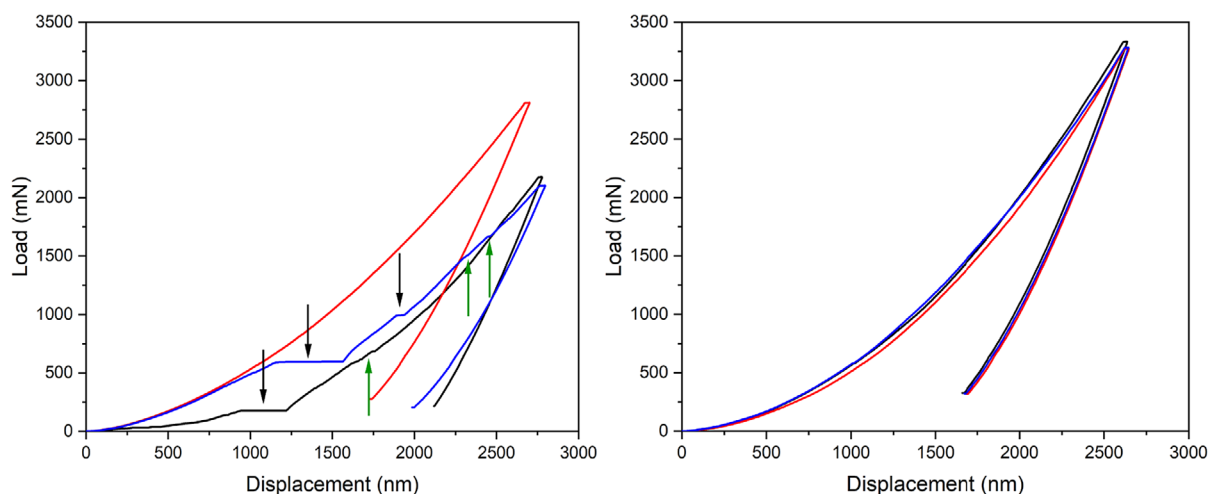

Figure 10. Load displacement curves of SiC/(Hf$_{0.75}$Ta$_{0.25}$)C(N)/C (left) and SiC/(Hf$_{0.75}$Ta$_{0.25}$)C(N)/(B)C (right). In the left figure, black arrows display major pop-in events and green arrows show minor events.

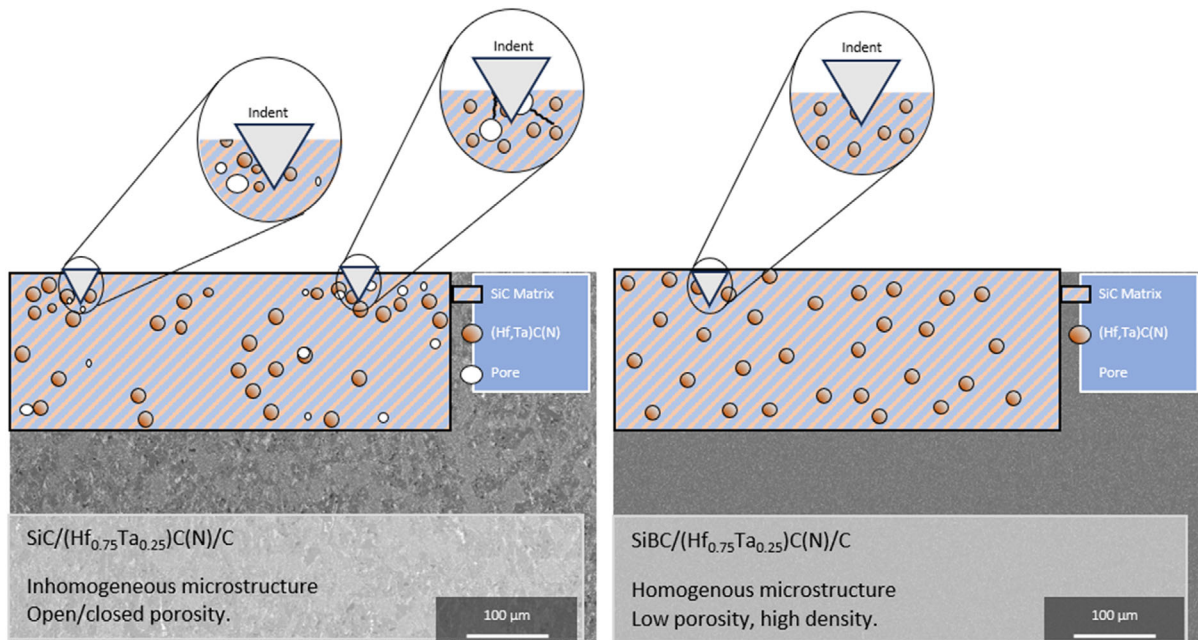**Figure 11.** SEM images and schematics with short descriptions are displayed (Left SiC/$(Hf_{0.75}Ta_{0.25})$C(N)/C, Right SiC/$(Hf_{0.75}Ta_{0.25})$C(N)/(B)C. On Top, a sketch of the nanoindentation experiment is displayed with the influence of the indent tip on the different samples.
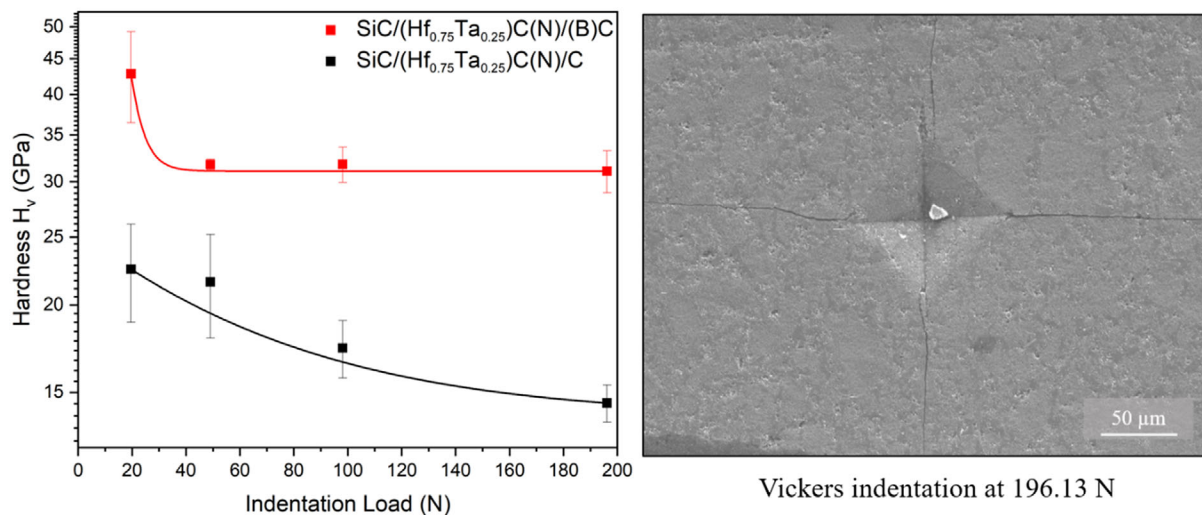

Figure 12. Vickers hardness of SiC/$(Hf_{0.75}Ta_{0.25})$C(N)/C and SiC/$(Hf_{0.75}Ta_{0.25})$C(N)/(B)C in the range 196.13 to 19.61 N (left) and SEM micrograph of a Vickers indent of SiC/$(Hf_{0.75}Ta_{0.25})$C(N)/(B)C at 196.13 N (right).

effect attributed to the presence of porosity within the material.[61,62] SiC/$(Hf_{0.75}Ta_{0.25})$C(N)/(B)C shows an entirely different course with a more pronounced horizontal asymptote at 31 GPa, initiating from 49.03 to 196.13 N. The hardness of the material in the macro scale is constant, and no indentation size effect was observed. However, the hardness vastly increases to 42.8 ± 6.4 GPa at a load of 19.61 N. This exceptionally high value is higher than that determined for most boron-free composites and is located between the super hard materials B_4C and c-BN.[8] This hardness is attributed to the low porosity, well-dispersed

fine grains acting as an effective impediment to dislocation mobility (analogous to precipitation hardening in conventional alloys), and the increased hardness of both silicon carbide and the (Hf,Ta)C(N) solid solution. Still, it is imperative not to consider the measurement error of 19.61 N. It is probable that somewhat inhomogeneous points were assessed in this instance, signifying that even though the boron-modified sample exhibits a favorable microstructure in comparison to the other sample, it still presents lower uniformity in phase distribution.

**ADVANCED
SCIENCE NEWS**

www.advancedsciencenews.com

**ADVANCED
ENGINEERING
MATERIALS**

www.aem-journal.com

3. Conclusion

The present study investigated the influence of the modification with minor amounts of boron on a composite material consisting of SiC/(Hf$_{0.75}$Ta$_{0.25}$)C(N)/C and represents the first study where the thermal properties and hardness of SiC/(Hf$_{0.75}$Ta$_{0.25}$)C(N)/(B)C composites were comprehensively examined—encompassing heat capacity, thermal diffusivity, thermal conductivity, Young's modulus, and macro hardness to the best of our knowledge.

Maintaining a low boron concentration (below 1 wt%) was crucial to enhance the microstructural evolution during sintering while preventing undesired transition metal borides. The strategic incorporation of boron into the ceramics was confirmed by elemental analysis, while Raman spectroscopy indicated that the boron is located in the segregated graphite phases. The advantageous effects on sintering yielded a highly dense sample with minimal porosity and a uniformly distributed microstructure. The homogeneous microstructure led to a reduction in thermal conductivity and an exceptionally high macro hardness of ≈31 GPa. Furthermore, the material exhibited a low thermal expansion coefficient and limited temperature dependence of thermal conductivity, rendering it a promising candidate for future high-temperature applications. In this context, to confirm suitability for (ultra) high-temperature applications, further studies in oxidative and corrosive environments at elevated temperatures are needed.

4. Experimental Section

Materials Preparation: The synthesis of SiC/(Hf,Ta)C(N)/(B)C composites followed the method described by Wen et al.[19] In this study, minor changes to the composition were made by adjusting the Hf:Ta ratio to 75:25 instead of 70:30. Additionally, to facilitate the sintering process, a small amount of boron was introduced.[63] The desired boron weight fraction was 0.2 to 0.5 wt% in order to achieve optimal densification without discontinuous growth of SiC grains.[63,64] In a typical approach, SiC/(Hf$_{0.75}$Ta$_{0.25}$)C(N)/(B)C and SiC/(Hf$_{0.75}$Ta$_{0.25}$)C(N)/C powders were synthesized by chemically modifying the preceramic polycarbosilane StarPCS SMP-10 (Starfire Systems, USA) with dimethylamine complexes of hafnium (TDMAH, Sigma-Aldrich, ≥99.99%) and tantalum (PDMAT, Sigma-Aldrich, ≥99.99%). The molar ratio of TDMAH:PDMAT was set to 75:25. For SiC/(Hf$_{0.75}$Ta$_{0.25}$)C(N)/(B)C, the precursor was additionally reacted with borane dimethylsulfide complex (BMS, Sigma-Aldrich), with a metal-to-boron molar ratio of 2:1. The reaction was carried out in toluene under Schlenk conditions. Further details of the synthesis procedure can be found in the aforementioned work.[19,31] The obtained solid and black-colored single-source precursors underwent pyrolysis under an argon atmosphere at 1000 °C and were subsequently ground to produce powders with a particle size less than 100 μm. The ceramic yield was approximately 80%. Monolithic samples were subsequently prepared SPS (FCT HP D 25/1 equipment, FCT Systeme GmbH, Frankenblick, Germany) at 2200 °C, applying a pressure of 50 MPa for 20 min under vacuum conditions. Heating and cooling rates were set at 100 °C min^{-1}.

Characterization: Composition and Microstructure: Regarding the characterization, X-ray diffraction (XRD) measurements were carried out for the powder samples in transmission mode and for the bulk samples in reflection mode using STADI MP (STOE, Darmstadt, Mo K-alpha source). Raman spectra were recorded using a micro-Raman HR8000 spectrometer (Horiba Jobin Yvon, Bensheim, Germany, 514.5 nm). Sample preparation for scanning electron microscopy (SEM) and transmission electron microscopy (TEM) followed a standard ceramographic procedure, including sample cutting, grinding, and final polishing steps. To achieve electron

transparency for TEM inspection, the polished TEM foil was Ar$^+$-ion milled until perforation occurred. In order to avoid sample charging under the incident electron beam, the SEM and TEM samples were coated with a thin carbon film. High-resolution scanning electron microscopy (HR-SEM) was conducted using a JSM-7600 F (JEOL Ltd., Tokyo, Japan). Backscattered electron (BSE) images were taken at an accelerating voltage of 15 keV. TEM analysis was performed using a JEM-2100 F (JEOL Ltd., Tokyo, Japan) operating at an accelerating voltage of 200 keV, equipped with an energy-dispersive X-ray spectroscopy (EDS) detector. The selected area electron diffraction (SAED) technique was utilized to gain structural information on the constituting phases within the sintered SiC/(Hf,Ta)C(N)/(B)C ceramic. Quantitative elemental analysis of Si, Hf, Ta, B, C, N, and O was carried out at Mikroanalytisches Labor Pascher (Remagen, Germany).

Thermal Analysis: Thermal expansion was determined with a DIL 402 E (NETZSCH-Gerätebau GmbH, Selb, Germany) in the range of RT-1500 °C using a heating rate of 5 °C min^{-1} under argon atmosphere (sample geometries: $10 \times 2.5 \times 2.5$ mm). Thermal diffusivity data were collected with a LFA 457 MicroFlash (NETZSCH-Gerätebau GmbH, Selb, Germany) from RT—900 °C under argon atmosphere. DSC experiments were carried out using a STA 449 F3 Jupiter (NETZSCH-Gerätebau GmbH, Selb, Germany) in the range of RT-900 °C using a heating rate of 10 °C min^{-1} under argon atmosphere.

Mechanical Properties: Macro Vickers hardness was tested using a Dia TEstor 2Rc (Otto Wolpert-Werke, Ludwigshafen Germany) with loads between 196.13 and 19.61 N. For nanoindentation, a G200 Nano indenter (KLA-Tencor) with a maximum load of 3000–3500 mN (average penetration depth of 2000–2500 nm) equipped with a Berkovich indenter tip was used to obtain average reduced Young's moduli. The Youngs's modulus was calculated from the reduced moduli (a Poisson's ratio of 0.3 was assumed). Density and open porosity were measured according to Archimedes method; skeletal porosity was estimated from SEM image data via quantitative image analysis using ImageJ software (National Institute of Health, USA).[36,65]

Conflict of Interest

The authors declare no conflict of interest.

Data Availability Statement

The data that support the findings of this study are available from the corresponding author upon reasonable request.

Keywords

precursor-derived ceramics, spark plasma sintering, thermomechanical properties of SiC-composites

[1] R. A. Andrievskii, N. S. Strel'nikova, N. I. Poltoratskii, E. D. Kharkhardin, V. S. Smirnov, *Powder Metall. Met. Ceram* **1967**, *6*, 65.

[2] E. Wuchina, E. Opila, M. Opeka, W. Fahrenholtz, I. Talmy, *Electrochem. Soc. Interface* **2007**, *16*, 30.

[3] W. G. Fahrenholtz, G. E. Hilmas, *Scr. Mater.* **2017**, *129*, 94.

[4] H. O. Pierson, in *Handbook of Refractory Carbides and Nitrides*, Elsevier, William Andrew Inc., Norwich, NY **1996**.

[5] H. K. M. Al-Jothery, T. M. B. Albarody, P. S. M. Yusoff, M. A. Abdullahr, A. R. Hussein, *IOP Conf. Ser.: Mater. Sci. Eng.*, **2020**, *863*, 012003.

[6] J. Binner, M. Porter, B. Baker, J. Zou, V. Venkatachalam, V. R. Diaz, A. D'Angio, P. Ramanujam, T. Zhang, T. S. R. C. Murthy, *Int. Mater. Rev.* **2020**, *65*, 389.

[7] R. Savino, M. de Stefano Fumo, D. Paterna, M. Serpico, *Aerosp. Sci. Technol.* **2005**, *9*, 151.

[8] R. Riedel, in *Handbook of Ceramic Hard Materials*, Wiley, Weinheim **2000**.

[9] L. E. Toth, in *Transition Metal Carbides and Nitrides*, Academic Press, New York **1971**.

[10] O. Cedillos-Barraza, S. Grasso, N. A. Nasiri, D. D. Jayaseelan, M. J. Reece, W. E. Lee, *J. Eur. Ceram. Soc.* **2016**, *36*, 1539.

[11] J. Zhang, S. Wang, W. Li, *J. Am. Ceram. Soc.* **2019**, *102*, 58.

[12] C. M. Carney, T. A. Parthasarathy, M. K. Cinibulk, *J. Am. Ceram. Soc.* **2011**, *94*, 2600.

[13] R. Tandon, H. Dumm, E. L. Corral, E. Corral, L. Ronald, K. P. Kotula, Ultra high temperature ceramics for hypersonic vehicle applications, USA **2006**.

[14] T. Glechner, O. E. Hudak, T. Wojcik, L. Haager, F. Bohrn, H. Hutter, O. Hunold, J. Ramm, S. Kolozsvári, E. Pitthan, D. Primetzhofer, H. Riedl, *Mater. Des.* **2021**, *211*, 110136.

[15] C. M. Carney, *J. Mater. Sci.* **2009**, *44*, 5673.

[16] A. Potanin, A. N. Astapov, Y. Pogozhev, S. I. Rupasov, N. V. Shvyndina, V. V. Klechkovskaya, E. A. Levashov, I. A. Timofeev, A. N. Timofeev, *J. Eur. Ceram. Soc.* **2021**, *41*, 34.

[17] E. Ionescu, S. Bernard, R. Lucas, P. Kroll, S. Ushakov, A. Navrotsky, R. Riedel, *Adv. Eng. Mater.* **2019**, *21*, 1900269.

[18] N. Jacobson, *Curr. Opin. Solid State Mater. Sci.* **2001**, *5*, 301.

[19] Q. Wen, Z. Yu, Y. Xu, Y. Lu, C. Fasel, K. Morita, O. Guillon, G. Buntkowsky, E. Ionescu, R. Riedel, *J. Mater. Chem. C* **2018**, *6*, 855.

[20] Q. Wen, R. Riedel, E. Ionescu, *Adv. Eng. Mater.* **2019**, *21*, 1800879.

[21] Z. Zhang, S. Fu, F. Aversano, M. Bortolotti, H. Zhang, C. Hu, S. Grasso, *Ceram. Int.* **2019**, *45*, 9316.

[22] C. Zhang, A. Gupta, S. Seal, B. Boesl, A. Agarwal, *J. Am. Ceram. Soc.* **2017**, *100*, 1853.

[23] H. Li, Y. Yu, B. Fang, P. Xiao, S. Wang, *J. Eur. Ceram. Soc.* **2022**, *42*, 4651.

[24] A. Nisar, C. Zhang, B. Boesl, A. Agarwal, *Ceram. Int.* **2023**, *49*, 783.

[25] M. Li, Q. Xu, L. Wang, *Key Eng. Mater.* **2012**, *512–515*, 635.

[26] N. N. Ngoepe, J. de Villiers, *J. Nucl. Mater.* **2013**, *438*, 88.

[27] R. R. Tummala, A. L. Friedberg, *J. Appl. Phys.* **1970**, *41*, 5104.

[28] J.-A. Yeom, Y.-W. Kim, *J. Eur. Ceram. Soc.* **2022**, *42*, 4076.

[29] Y. Kodera, H. Kotera, T. Yamamoto, M. Ohyanagi, Z. A. Munir, *Phys. Status Solidi* **2006**, *3*, 2876.

[30] R. Vaben, D. Stöver, *Philos. Mag. B* **1997**, *76*, 585.

[31] Q. Wen, Y. Xu, B. Xu, C. Fasel, O. Guillon, G. Buntkowsky, Z. Yu, R. Riedel, E. Ionescu, *Nanoscale* **2014**, *6*, 13678.

[32] S. Kaur, G. Mera, R. Riedel, E. Ionescu, *J. Eur. Ceram. Soc.* **2016**, *36*, 967.

[33] L. G. Cançado, A. Jorio, E. H. M. Ferreira, F. Stavale, C. A. Achete, R. B. Capaz, M. V. O. Moutinho, A. Lombardo, T. S. Kulmala, A. C. Ferrari, *Nano Lett.* **2011**, *11*, 3190.

[34] A. Cuesta, P. Dhamelincourt, J. Laureyns, A. Martínez-Alonso, J. Tascón, *Carbon* **1994**, *32*, 1523.

[35] J. S. Burgess, C. K. Acharya, J. Lizarazo, N. Yancey, B. Flowers, G. Kwon, T. Klein, M. Weaver, A. M. Lane, C. Heath Turner, S. Street, *Carbon* **2008**, *46*, 1711.

[36] S. Saraf, A. Singh, B. G. Desai, *ASEG Ext. Abstr.* **2019**, *2019*, 1.

[37] W. D. KINGERY, *J. Am. Ceram. Soc.* **1959**, *42*, 617.

[38] Z. Li, R. C. Bradt, *J. Mater. Sci.* **1986**, *21*, 4366.

[39] I. G. Barantseva, V. N. Paderno, in *Refractory Carbides* (Ed: G. V. Samsonov), Springer, New York, NY **1974**, p. 283.

[40] S. Hiroshige, I. Takayoshi, I. Masahiko, *J. Nucl. Mater.* **1973**, *48*, 247.

[41] K. Becker, *Z. Physik* **1926**, *40*, 37.

[42] N. M. Sultan, T. M. B. Albarody, H. K. M. Al-Jothery, M. A. Abdullah, H. G. Mohammed, K. O. Obodo, *Materials* **2022**, *15*, 6229.

[43] C. K. Jun, P. Shaffer, *J. Less-Common Met.* **1971**, *24*, 323.

[44] J. B. Nelson, D. P. Riley, *Proc. Phys. Soc.* **1945**, *57*, 477.

[45] C. Stabler, A. Reitz, P. Stein, B. Albert, R. Riedel, E. Ionescu, *Materials* **2018**, *11*, 279.

[46] A. K. Collins, M. A. Pickering, R. L. Taylor, *J. Appl. Phys.* **1990**, *68*, 6510.

[47] D. S. Smith, A. Alzina, J. Bourret, B. Nait-Ali, F. Pennec, N. Tessier-Doyen, K. Otsu, H. Matsubara, P. Elser, U. T. Gonzenbach, *J. Mater. Res.* **2013**, *28*, 2260.

[48] A. L. Loeb, *J. Am. Ceram. Soc.* **1954**, *37*, 96.

[49] L. Silvestroni, A. Bellosi, C. Melandri, D. Sciti, J. X. Liu, G. J. Zhang, *J. Eur. Ceram. Soc.* **2011**, *31*, 619.

[50] S. Hayun, V. Paris, R. Mitrani, S. Kalabukhov, M. P. Dariel, E. Zaretsky, N. Frage, *Ceram. Int.* **2012**, *38*, 6335.

[51] M. Balog, P. Šajgalík, M. Hnatko, Z. Lenčéš, F. Monteverde, J. Kečkéš, J.-L. Huang, *J. Eur. Ceram. Soc.* **2005**, *25*, 529.

[52] X. Zhang, G. E. Hilmas, W. G. Fahrenholtz, *Mater. Sci. Eng.,: A* **2009**, *501*, 37.

[53] C. J. Smith, X.-X. Yu, Q. Guo, C. R. Weinberger, G. B. Thompson, *Acta Mater.* **2018**, *145*, 142.

[54] D. Demirskyi, H. Borodianska, T. Nishimura, T. S. Suzuki, K. Yoshimi, O. Vasylkiv, *J. Am. Ceram. Soc.* **2021**, *105*, 512.

[55] Z. Li, R. C. Bradt, *J. Mater. Sci.* **1987**, *22*, 2557.

[56] Z. Z. Fang, X. Wang, T. Ryu, K. S. Hwang, H. Y. Sohn, *IJRMHM* **2009**, *27*, 288.

[57] S. Yu, Q. Zeng, A. R. Oganov, G. Frapper, L. Zhang, *PCCP* **2015**, *17*, 11763.

[58] W. C. Oliver, G. M. Pharr, *J. Mater. Res.* **1992**, *7*, 1564.

[59] D. J. Oliver, B. R. Lawn, R. F. Cook, M. G. Reitsma, J. E. Bradby, J. S. Williams, P. Munroe, *J. Mater. Res.* **2008**, *23*, 297.

[60] V. Domnich, Y. Gogotsi, S. Dub, *Appl. Phys. Lett.* **2000**, *76*, 2214.

[61] R. W. Rice, in *Porosity of Ceramics: Properties and Applications*, CRC Press, Boca Raton, FL **1998**.

[62] M. Shahedi Asl, B. Nayebi, A. Motallebzadeh, M. Shokouhimehr, *Compos. Part B* **2019**, *175*, 107153.

[63] L. Stobierski, A. Gubernat, *Ceram. Int.* **2003**, *29*, 355.

[64] K. Raju, D.-H. Yoon, *Ceram. Int.* **2016**, *42*, 17947.

[65] M. Lau, F. Morgenstern, R. Hübscher, A. Knospe, M. Herrmann, M. Döring, W. Lippmann, *Prakt. Metallogr.* **2020**, *57*, 752.